

Numerical study of the time-reversal effects on super-resolution in random scattering media and comparison with an analytical model

T. Chan , S. Jaruwatanadilok , Y. Kuga & A. Ishimaru

To cite this article: T. Chan , S. Jaruwatanadilok , Y. Kuga & A. Ishimaru (2008) Numerical study of the time-reversal effects on super-resolution in random scattering media and comparison with an analytical model, Waves in Random and Complex Media, 18:4, 627-639, DOI: [10.1080/17455030802244286](https://doi.org/10.1080/17455030802244286)

To link to this article: <http://dx.doi.org/10.1080/17455030802244286>



Published online: 13 Oct 2008.



Submit your article to this journal 



Article views: 52



View related articles 



Citing articles: 2 View citing articles 

Full Terms & Conditions of access and use can be found at
<http://www.tandfonline.com/action/journalInformation?journalCode=twrm20>

Numerical study of the time-reversal effects on super-resolution in random scattering media and comparison with an analytical model

T. Chan, S. Jaruwatanadilok*, Y. Kuga and A. Ishimaru

Department of Electrical Engineering, University of Washington, Seattle, USA

(Received 25 February 2008; final version received 27 May 2008)

The time-reversal effects on super-resolution in random scattering media are analysed using numerical finite-difference time-domain (FDTD) simulations. The analytical solutions and results have been presented previously in the literature, which provide confirmation of spot-size reduction and also explanations of the shower curtain effects and backscattering enhancement. However, the analytical solutions are based on several approximations. Thus, validation of the analytical results against realistic scattering events is necessary. Two-dimensional FDTD Monte Carlo simulations have been employed for this investigation to simulate wave propagation and scattering in a random medium. The scattering environments are created by randomly locating cylindrical rods in the background medium. The simulation process involves a point source emitting a Gaussian pulse wave that propagates through the scattering medium, gets time-reversed, and then back-propagated into the same scattering medium. The focusing behaviours including the location of the focal point and its spot-size as a function of its transverse position are analysed. The shower curtain, particle size, and time domain effects are also investigated. In comparison, the behaviours of focusing derived by numerical results are consistent with those of previously reported analytical results. However, there are some differences, which we speculate to be mainly because of the different phase functions.

1. Introduction

In recent years, time-reversal has attracted considerable attention, owing to its potential applications, which include communication and imaging through complex environments. The concept of time-reversal is summarised as follows. When a wave is emitted by point source and received by an array of receivers, if the wave is then time-reversed and back-propagated into the same medium, the wave will refocus around the area of the original point source. How well the wave refocuses, or the beam width of various analysed signal responses, provides a measure for the resolution of the system.

Interesting applications of the time-reversal technique for communication and detection have been discussed in [1, 2, 3]. Jian et al. [1] discusses single antenna target detection using broadband frequency selection time-reversal. The research by Yun and Iskander [2] focus on the characterisation of the time-reversal technique in indoor multi-path environments such as hallways, the multiple reflection and transmission of slab walls, the diffraction from edges, and the scattering from various small structures. Lerosey et al. [3] discuss far-field time reversal and its application to telecommunications. On the medical imaging side, Fink et al. [4] proposed and demonstrated the application of locating and focusing a reflecting target, such as a kidney stone,

*Corresponding author. Email: sermsak@ee.washington.edu

using ultrasonic time-reversal techniques. Similar to research done in this report, Liu et al. [5] did an experimental study on electromagnetic time-reversal in highly scattering environments, with a focus on performance when environmental conditions change. The experimental results, found using electromagnetic time-reversal measurements and performed using a vector network analyser, are compared with theoretical predictions. While most of these papers focus primarily on the different applications and theoretical aspects of time-reversal theory, our paper presents a detailed numerical study of time-reversal in discrete random media.

The focus of this paper is to conduct realistic numerical simulations that investigate time-reversal focusing and verify the work done by Ishimaru et al. [6]. It is known that in free space, the time-reversed pulse will be refocused with a resolution largely determined by the array aperture size. However, when time-reversal is used in a random medium, the wave will be refocused with a better resolution than that of free space because of the multiple scattering effect. This phenomenon is termed ‘super-resolution,’ and is due to the coherence length, which can be smaller than the free space spot size. Thus, increasing multiple scattering will result in decreased spot size and super-resolution.

2. Time-reversal focusing analysis based on the two-frequency mutual coherence function

The detailed derivation of the analytical solution is presented in [6]. In this section, we will provide a brief description of the analytical solution and the approximations and assumptions used for obtaining this analytical solution. These will be critical for understanding the difference between the numerical and analytical results. The geometry of the analytical model formulation is shown in Figure 1. A point source at \bar{r}_t emits a Gaussian pulse $f(t)$ ($F(\omega)$ in frequency domain) described by

$$f(t) = A_o \exp\left(-\frac{t^2}{T_o^2} - i\omega_o t\right) \Leftrightarrow F(\omega) = A_o \frac{2\sqrt{\pi}}{\Delta\omega} \exp\left(-\frac{(\omega - \omega_o)^2}{\Delta\omega^2}\right) \quad (1)$$

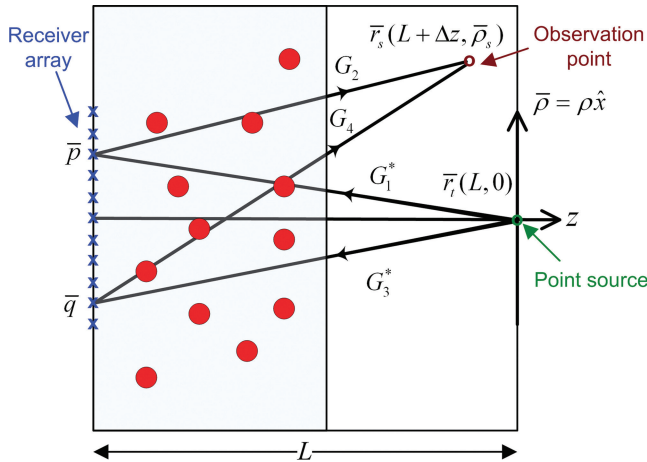


Figure 1. Geometry of the problem: a point source at \bar{r}_t emits a Gaussian pulse, which is received by $2M + 1$ receivers, time-reversed, back-propagated into the same medium and observed at \bar{r}_s . $p = mh_o$, $q = nh_o$, $h_o = \lambda_o/2$.

where $\Delta\omega = 2/T_o$ is the bandwidth and ω_o is the carrier frequency. The signal is received by an array of $2M + 1$ elements, time-reversed, and back-propagated into the same medium and observed at \bar{r}_s . The analytical solution of the average field and average intensity requires the derivation of the mutual coherent function [5]. The average field is therefore given by

$$\langle \psi(\bar{r}_s, t) \rangle = \frac{1}{2\pi} \int \exp(-i\omega t) d\omega \sum_m \Gamma_m(\bar{r}_s, \bar{r}_m, \bar{r}_t, \omega) F^*(\omega) \quad (2)$$

where $\Gamma_m = \langle G_2(\bar{r}_s, \bar{r}_m, \omega) G_1^*(\bar{r}_m, \bar{r}_t, \omega) \rangle$ is the mutual coherent function of the field at \bar{r}_s and \bar{r}_t with the source at \bar{r}_m . The function $G_1(\bar{r}_m, \bar{r}_t, \omega)$ is the Green's function of a wave with frequency ω observed at \bar{r}_s from the source at \bar{r}_t . The symbol * denotes complex conjugate. The average intensity is given by the second moment $\langle \psi(\bar{r}_s, t_1) \psi^*(\bar{r}_s, t_2) \rangle$

$$\langle \psi(\bar{r}_s, t_1) \psi^*(\bar{r}_s, t_2) \rangle = \frac{1}{(2\pi)^2} \int d\omega_1 d\omega_2 \Gamma(\omega_1, \omega_2) F_1(\omega_1) F_2^*(\omega_2) \exp(-i\omega_1 t_1 + i\omega_2 t_2) \quad (3)$$

where $\Gamma(\omega_1, \omega_2) = \sum_m \sum_n \langle G_1^* G_2 G_3 G_4^* \rangle$, $G_1 = G(\bar{p}, \bar{r}_t, \omega_1)$, $G_2 = G(\bar{r}_s, \bar{p}, \omega_1)$, $G_3 = G(\bar{q}, \bar{r}_t, \omega_2)$, and $G_4 = G(\bar{r}_s, \bar{q}, \omega_2)$. Notice that this requires knowledge of the fourth-order moment $\langle G_1^* G_2 G_3 G_4^* \rangle$. The detailed calculations of the mutual coherent function Γ_m and $\Gamma(\omega_1, \omega_2)$ are presented in [6] and will not be discussed here. However, it is important to note that there are a few approximations which make the analytical solution tractable. First, the Green's functions are assumed to be the circular complex Gaussian random functions [7]. Then, the fourth-order moment can be reduced to the second-order moment as

$$\langle G_1^* G_2 G_3 G_4^* \rangle = \langle G_1^* G_2 \rangle \langle G_3 G_4^* \rangle + \langle G_1^* G_3 \rangle \langle G_2 G_4^* \rangle - \langle G_1^* \rangle \langle G_2 \rangle \langle G_3 \rangle \langle G_4^* \rangle \quad (4)$$

Second, the free space Green's function is written using parabolic approximation, in which the distance between a wave emitted at $(L, 0)$ and observed at $(p, 0)$, normally expressed as $(L^2 + p^2)^{1/2}$ is approximated by $L + p^2/L$.

The scattering characteristic of the random scattering medium is captured by the phase function of the scattering pattern of a single scatterer $p(s)$. In the analytical solution, $p(s)$ is assumed to be Gaussian given by

$$p(s) = 4\alpha_p \exp(-\alpha_p s^2) \quad (5)$$

where $s = 2 \sin(\theta/2)$, θ is the scattering angle. α_p characterises the angular distribution of the phase function. It relates to the mean cosine $\bar{\mu}$ as

$$\alpha_p = \frac{\bar{\mu} \ln(2)}{(1 - \bar{\mu})^2 (2^{2/3} - 1)} \quad (6)$$

Although the Gaussian phase function does not represent an accurate phase function for a realistic scattering event, it is used for obtaining a numerically attainable solution. In practice, the phase function is more complicated and includes side lobes as shown in Figure 4 (see later).

As the derived analytical solutions are based on several assumptions and Green's function approximations, validation of these analytical results against numerical simulation techniques, such as finite-difference time-domain (FDTD), is necessary. In addition, because FDTD is based

on Maxwell's equation solution, the FDTD simulations offer closer approximations to the multiple scattering natures of random scattering media.

3. FDTD simulations

3.1. Simulation set-up

A diagram of the numerical simulation set up is given in Figure 2. The numerical simulations attempt to emulate the geometry of that of the analytical formulation. Note that the diagram is not completely drawn to scale. d is defined as the distance between the point source and the random media and the actual simulation consists of 21 array receivers that are $\lambda/2$ apart. The random scattering media are randomly located dielectric cylinders.

The two-dimensional (2D) FDTD model shown in Figure 2 is surrounded by a 2λ -thick uniaxial perfectly matched layer (UPML). This means that all out-going waves will propagate outward without physical reflection from the boundary. The UPML, which employs an anisotropic perfectly matched medium, will absorb all the waves that hit the boundary. The emitted pulse at the point source has a centre of frequency of 100 GHz; thus, the wavelength in free space λ is 3 mm. For the numerical simulations, the Gaussian modulated pulse is modified slightly. To simplify the simulation and calculation process, only the real part of the function in (1) is used and A_o is set to 1. Also, as the computational domain is relatively large, the function T_o is modified to $3T_o$ to increase the initial bandwidth of the Gaussian pulse to be emitted from the point source. A newly modified $f(t)$ used in the numerical simulations is given by Equation (7).

$$f(t) = \exp\left(-\frac{t^2}{(3 \cdot T_o)^2}\right) \cdot \cos(\omega_o t) \quad (7)$$

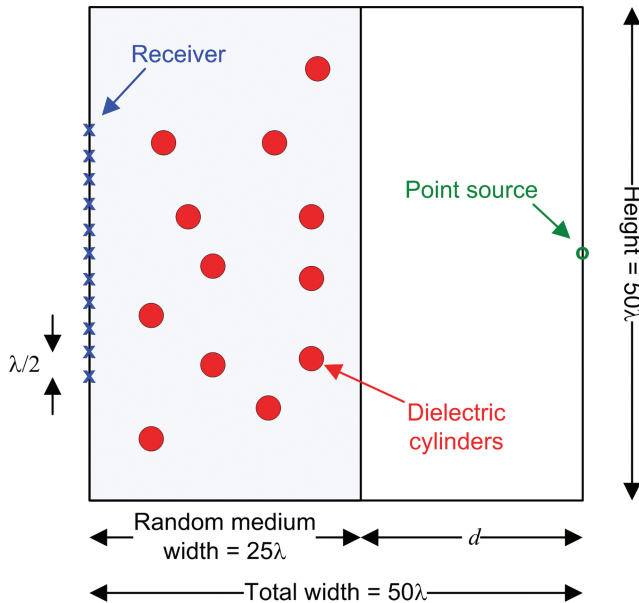


Figure 2. Diagram of the numerical simulation set-up.

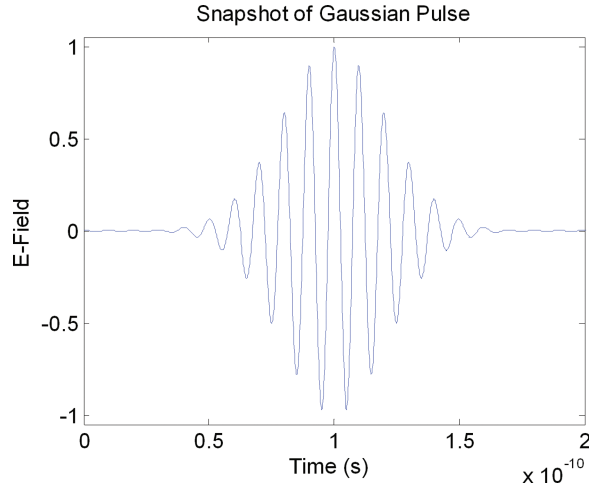


Figure 3. Snapshot of Gaussian pulse in time domain.

Each of the cylinders will have a dielectric constant given by $\varepsilon_r = 4.5 - 0.01j$, which represents a low-loss glass material at microwave frequency. The imaginary part of ε_r represents the loss; however, for a low-loss material, this value is difficult to measure because the inverted value can be substantially different. In order to evaluate its effect, we conducted numerical simulations using two different values of ε_r ($\varepsilon_r = 4.5 - 0.02j$ and $\varepsilon_r = 4.5 - 0.001j$), and the results are essentially the same in our case.

The edges of each of the cylinders will be approximated using a cylinder staircase approximation. As the diameter of each cylinder is about 3.33λ and the size of each grid is about $\lambda/30$, the grid size is sufficiently small to still get very accurate numerical simulation results. A snapshot of the Gaussian pulse in the time-domain is shown in Figure 3.

3.2. Phase function of dielectric cylinders

We employ randomly located dielectric cylinders to create the scattering effects. From Ruck et al. [8], the differential cross section for a homogenous dielectric cylinder is given by (8). The subscripts 0 and 1 refer to free space and the cylinder, respectively, and a is the radius of a cylinder. The angle θ refers to the difference between the incident and scattering angles such that $\theta = 0$ and $\theta = \pi$ refer to backward and forward scattering, respectively.

By plotting the differential cross section of a dielectric cylinder as a function of θ , the phase function can be plotted. Figure 4 compares the Gaussian phase function with an anisotropic factor, $\alpha_p = 44(\bar{\mu} = 0.85)$, which is used in the analytical solution, to the phase function of a cylinder, which is used for random media calculations in the numerical solution. When $\bar{\mu}$ is large, the scattering characteristics are often dominated by the strong main lobe of the phase function; therefore, the best fit is obtained from main lobe comparisons. As can be seen from the plot, for $ka = 10(\bar{\mu} = 0.77)$ where $k = 2\pi/\lambda$, there is a relatively good match between the analytical and numerical phase functions on the main lobe. The extra side lobes in the phase function for the cylinder represent the realistic nature of the scattering. This aspect is missing when using a

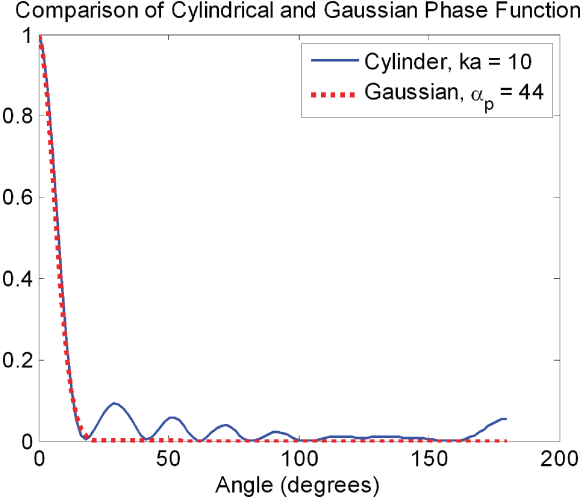


Figure 4. Comparison of the phase function of cylinders and Gaussian phase functions.

Gaussian phase function

$$\begin{aligned} \sigma_d &= \frac{2}{\pi k_0} \left| \sum_{n=0}^{\infty} \varepsilon_n (-1)^n A_n \cos n\theta \right|^2 \\ A_n &= -\frac{(k_1/\mu_1) J_n(k_0a) J'_n(k_1a) - (k_0/\mu_0) J'_n(k_0a) J_n(k_1a)}{(k_1/\mu_1) H_n^{(1)}(k_0a) J'_n(k_1a) - (k_0/\mu_0) H_n'^{(1)}(k_0a) J_n(k_1a)} \\ \varepsilon_n &= \begin{cases} 1 & \text{for } n = 0 \\ 2 & \text{for } n = 1, 2, 3, \dots \end{cases} \end{aligned} \quad (8)$$

The relationship between the differential cross section σ_d and the total cross section σ_t is given by the following relationship [9]

$$\int_{4\pi} \sigma_d d\omega = \frac{\sigma_t}{4\pi} \int_{4\pi} p(\hat{0}, \hat{i}) d\omega \quad (9)$$

where $d\omega$ is the differential solid angle and $p(\hat{0}, \hat{i})$ is the phase function. From (9), σ_t , which is used in the numerical optical depth (OD) calculation, can be calculated. For $ka = 10$ and frequency = 100 GHz, the total cross-section σ_t is 0.0274 m^2 . The length of the random medium is $L = 25\lambda = 0.075 \text{ m}$. The random medium computational area is $L \times H = 25\lambda \times 50\lambda = 0.01125 \text{ m}^2$. The appropriate number of particles in the computational domain can be calculated for a given optical depth τ . As $\tau = \rho \sigma_t L$, the appropriate number of particles for each optical depth can be found by multiplying the number density ρ ($\rho = \tau / \sigma_t L$) by the random medium computational area $L \times H$. Table 1 summarises the relevant random medium calculations.

3.3. Spatial and time focusing in stationary and non-stationary random media

We investigate spatial and time focusing of a short pulse in random media by time-reversal. A few snapshots of 2D field strength are presented in Figures 5 and 6. Figure 5 shows the time-reversal effect for a wave that travels through free space. Figure 5(a) is a snapshot of the wave as it travels

Table 1. Summary of random media calculations.

Optical depth	Number density (m^{-3})	Approximate number of particles	Fractional volume (%)
1	487	5 and 6	3.82
2.5	1217	14	9.77
5	2433	27	18.85
7.5	3950	41	28.62
10	4866	55	38.40

unimpeded and freely through a free space media. Figure 5(b) shows the refocused wave around the area of the original point source after the incoming wave from Figure 5(a) was time-reversed and back-propagated in the same free-space medium.

Figure 6 shows the time-reversal effect for a wave that travels through a random medium. To create this random medium, seven randomly located dielectric cylinders, with a radius of 0.67λ are placed in a random computational domain 2λ away from the point source. Figure 6(a) shows an initial Gaussian wave emitted from the point source hitting the random medium causing multiple scattering, as expected. When the time-reversed wave from Figure 6(a) is back-propagated into the same random media from which it was sent, the result is super-resolution around the area of the original point source as shown in Figure 6(b). However, when the time-reversed wave from Figure 6(c) is back-propagated in a non-stationary random medium, the wave never converges or refocuses anywhere; super-resolution does not occur. This demonstrates that the random medium has to be stationary for super-resolution to occur. In this case, the non-stationary random medium is defined by the change of location of scattering objects when the time-reversed wave propagates back into the random medium. In FDTD simulations, we simply generate another random location of scattering objects with the same number of objects.

3.4. Lateral resolution for time-reversal focusing: comparison with analytical solution

Next, we investigate the lateral resolution in several cases and compare them with that of the analytical results reported in [6]. Time domain data is collected and analysed at the original point source for a time period T_p . T_p can be arbitrarily chosen, however, the value should be large enough to cover all the multiple scattering from the random media objects. Thus, when the number of objects in the random medium increases, the T_p value is adjusted accordingly. Spatial domain data is collected and analysed in the transverse direction along the dashed line (16 λ long), shown in Figure 7, at a specific time t_s . This t_s value is determined at the time when the point source E-field value is maximised in the time domain.

For each optical depth, 10 Monte Carlo simulations of the random medium are performed, and the averages of these simulations are taken. However, for optical depth of 1, the calculated

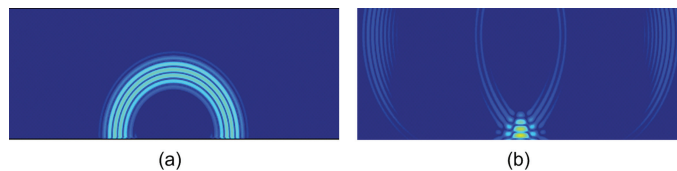


Figure 5. Snapshots in free-space media. (a) Gaussian pulse propagating through free space. (b) Time-reversed pulse refocused near original point source.

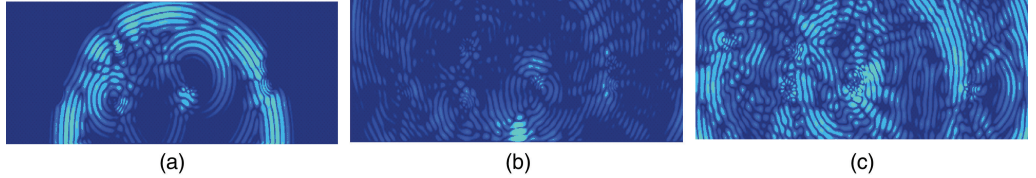


Figure 6. Snapshots in random media. (a) Gaussian pulse propagating through random media. (b) Time-reversed pulse back-propagated in stationary random media (c) Time-reversed pulse back-propagated in non-stationary random media.

number of particles is 5.47; thus, 10 simulations are run with five particles ($OD = 0.913$) and nine simulations are run with six particles ($OD = 1.096$). The average of these 19 simulations should produce the most accurate $OD = 1$ data. The number of particles approximated for the other optical depths calculates to values less than 5% of the desired optical depth number; thus, the average of 10 simulations for these optical depths is sufficient to give accurate results. Each Monte Carlo simulation contains a different set of randomly located cylinders within the random computational media. Figure 8 plots the average normalised E-field magnitude, $\langle |E| \rangle$ as a function of the transverse position, in terms of wavelength. The ensemble average is denoted by $\langle \cdot \rangle$. The free-space data is given by the curve on the outside and as the optical depth increases from 1 (dotted) to 5 (circle) to 10 (dot-dash), the beam width gets smaller, and the resolution gets better.

Very similar results are achieved when plotting the average normalised intensity $\langle |E|^2 \rangle$ as a function of the transverse position, shown in Figure 9. The main difference is that for each optical depth, the beam width is smaller and the side lobes are reduced. Figure 10 compares the analytical results obtained using Equations (2) and (3) to the FDTD simulations. The outer curves represent the analytical data, while the dotted curves represent the numerical data. While the analytical data do not completely match the numerical data, which is likely owing to differences in the Gaussian phase function and phase function for the cylinder, the two sets of data are consistent with one another in that as the optical depth is increased, so does the resolution.

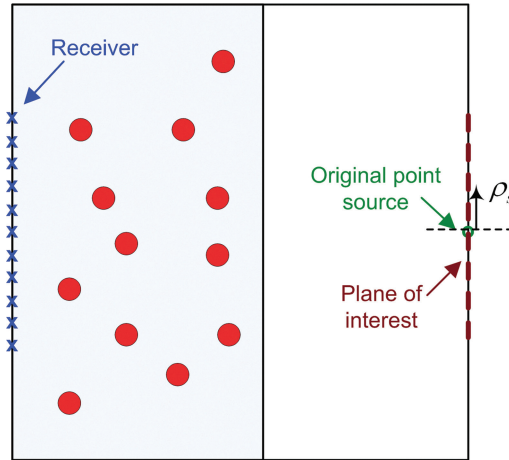


Figure 7. Collecting spatial and time domain data.

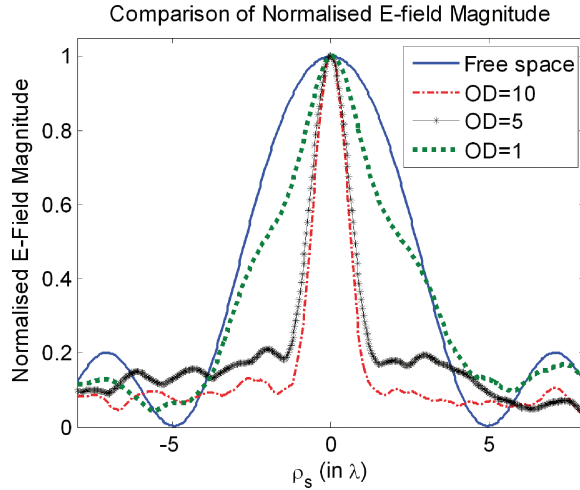


Figure 8. Normalised field versus. transverse position for different optical depths (OD).

3.5. Shower curtain effect and the anisotropic factor

If multiple scattering is increased, the coherence length decreases proportional to the inverse of the square root of the scattering depth, resulting in a smaller spot size. This formulation gives the shower curtain effect, which gives a higher resolution when the random medium is closer to the source. In this section, we investigate this phenomenon and the effect of the anisotropic factor α_p on spot size reduction. Figures 11 and 12 plot the beam width as functions of the optical depth. Figure 11 analyses the numerical shower curtain effects. d is defined as the distance between the point source and the random medium (Figure 2). The circle data points represent $d = 25\lambda$ as this distance decreases, eventually to $d = 0$ as shown by the square data points, the beam width gets smaller, and the resolution gets better. Figure 12 analyses the effect of the anisotropic factor by changing the size of the cylinders. The triangle data points represent a cylindrical radius of

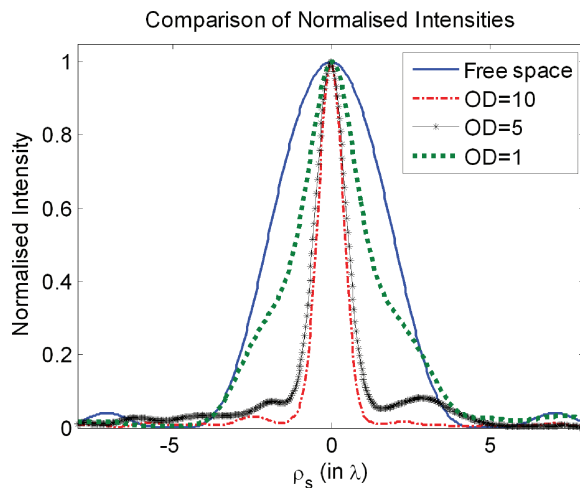


Figure 9. Normalised intensity versus transverse position for different optical depths (OD).

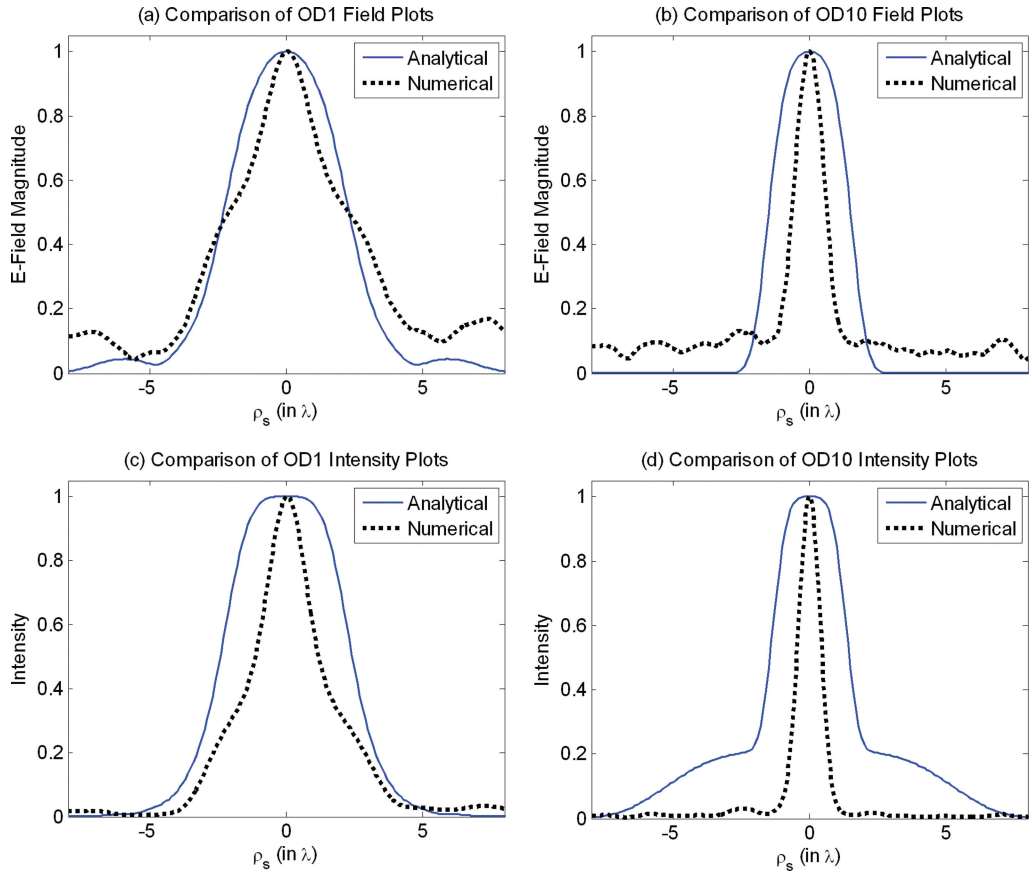


Figure 10. Comparison of analytical to numerical results. (a), (b) OD = 1 and OD = 10 field comparison plots. (c), (d) OD = 1 and OD = 10 intensity comparison plots.

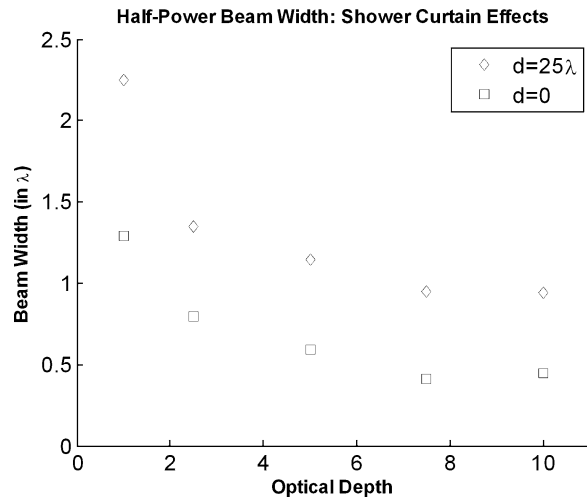


Figure 11. Numerical shower curtain effects. OD: optical depth, d: distance between point source and random medium.

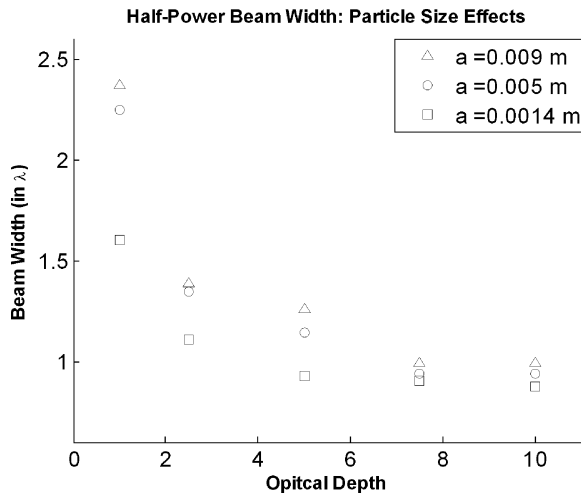


Figure 12. Numerical particle size effects. OD: optical depth, a: radius of cylinder.

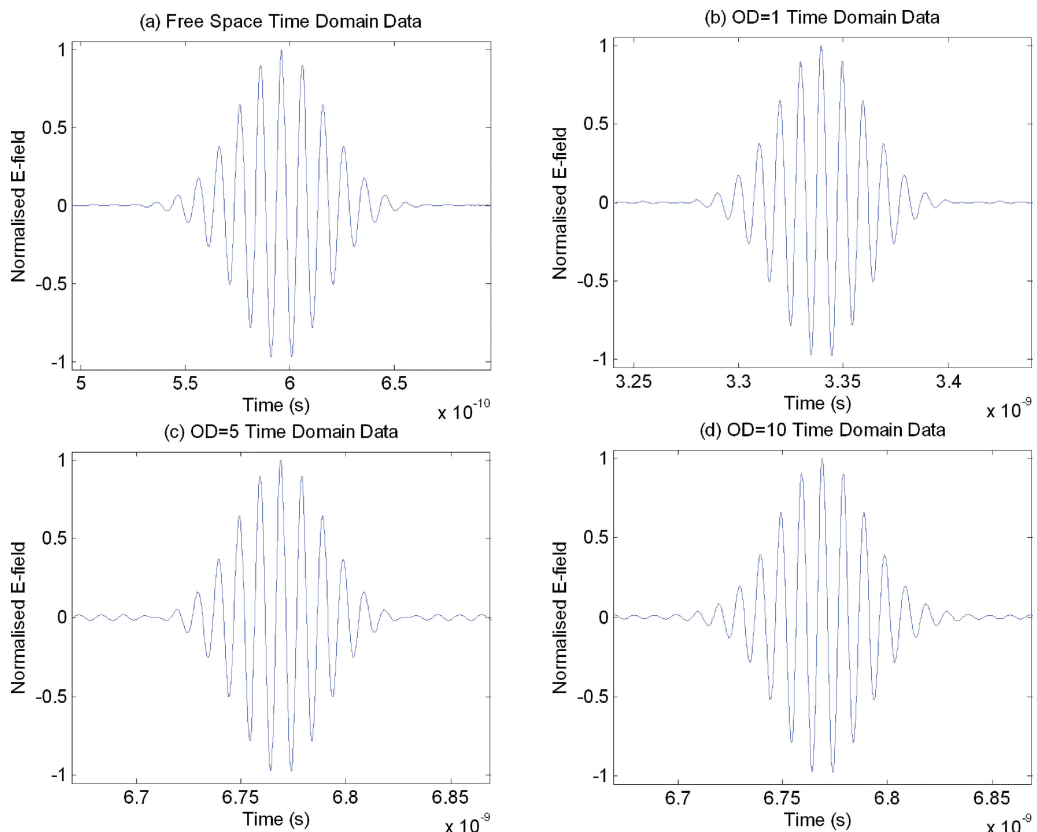


Figure 13. Numerical time domain data. (a), (b), (c), and (d) Time domain data for free-space, OD = 1, OD = 5, and OD = 10, respectively. Length of each time axis is 0.2 ns.

$a = 0.009$ m ($\bar{\mu} = 0.78$). As this value decreases to $a = 0.005$ m ($\bar{\mu} = 0.77$), represented by the circle data points, or $a = 0.0014$ m ($\bar{\mu} = 0.35$), represented by the square data points, the beam width gets smaller, and the resolution gets better. Both numerical shower curtain and particle size effects are consistent with the analytical data.

3.6. Time domain behaviours

Figure 13 summarises the time domain E-field data collected for free space media and random media with different optical depths. The length of time axis for each for each plot is set at 0.2 ns to keep the data consistent. As can be seen, for free space, and for the different optical depths, the time domain data have identical characteristics and all look very similar to the original Gaussian pulse that was emitted from the point source (Figure 3). As for a comparison, Ishimaru's paper [5] did contain some analytical plots in the time domain. For these plots, the pulse width of the field plots for different optical depths are essentially identical, which is consistent with the numerical time domain results shown in Figure 13.

The snapshots of Figure 6 showed that the random medium has to be stationary in order for super-resolution to occur. Figure 14 provides plots that will validate this claim. Figures 14(a) and (c) represent the time and spatial domain data, respectively, for a time-reversed wave that is back propagated in the same random medium in which it was sent in. Figures 14(b) and (d) represent

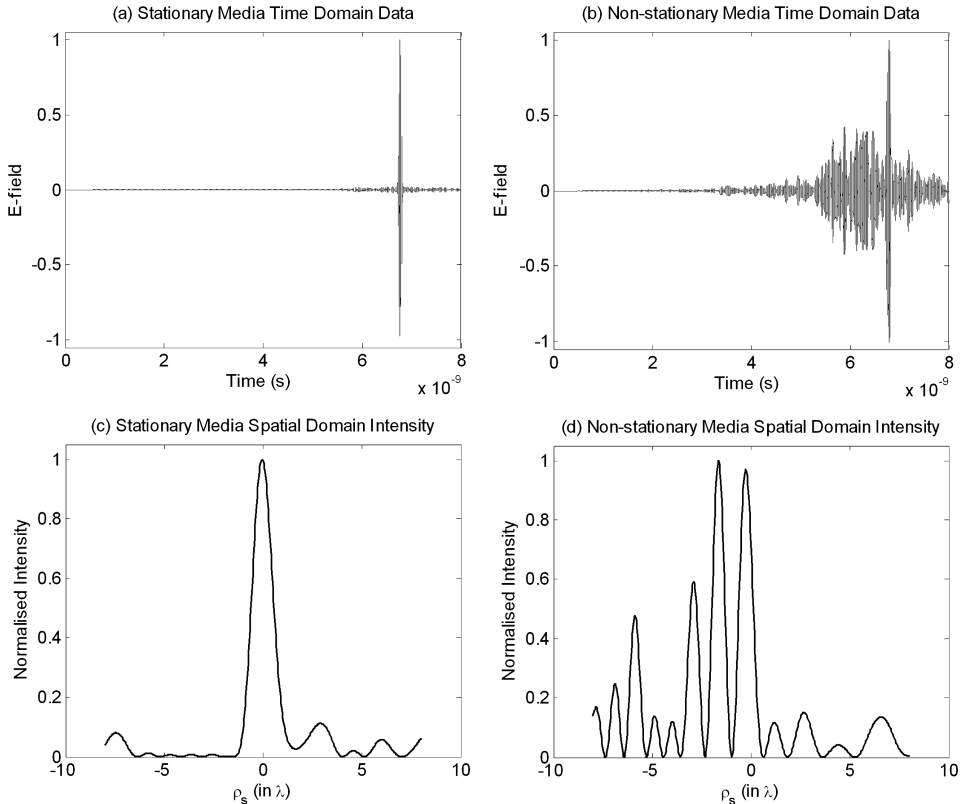


Figure 14. Stationary and non-stationary focusing in random media. (a),(c) Stationary random media time and spatial domain data. (b),(d) Non-stationary random media time and spatial domain data.

the time and spatial domain data, respectively, for a time-reversed wave that is back propagated in a different random medium from which it was sent it. The differences between the two sets of data can easily be recognised. In Figure 14(a), there is only one clear and distinguishable pulse in the time domain, and in Figure 14(c), there is a clear focused beam with high intensity at the location of the original point source. In Figures 14(b) and (d), there is no real distinguishable pulse in the time domain and there are multiple beams along the transverse position of the spatial domain. This data shows that the time-reversed wave never gets refocused and super-resolution never occurs in this scenario.

4. Conclusions

This paper presents a numerical study of the time-reversal in random media based on the FDTD method. An important finding is that the behaviours of super-resolution focusing by time-reversal are consistent with the prediction from analytical solutions. Increasing the optical depth (number of particles), decreasing the anisotropic factor (particle size), and decreasing the distance between the random medium domain and the source, all result in a decreased beam spot size and thus increased resolution. However, the numerical 2D-FDTD Monte Carlo simulations are not completely identical to the analytical results, which is likely owing to the approximations of the analytical solutions and differences in Gaussian phase function and the phase function of the cylinders. Another interesting observation is that super-resolution focusing only occurs in stationary random media when the time-reversed backscattered wave encounters the exact same random media.

Acknowledgements

This work was supported by the Office of Naval Research (N00014-07-1-0428) and the National Science Foundation (ECS0601394).

References

- [1] Y. Jian, J.-G. Zhu, D.D. Stancil, J. Moura, A.G. Cepni, B. Henty, and Y. Jin, Single antenna target detection using broadband frequency selection time-reversal method, *APS/URSI Symposium*, Albuquerque, NM, 2006.
- [2] Z. Yun and M.F. Iskander, Time-reversal with single antenna systems in indoor multipath environments: Spatial focusing and time compression, *APS/URSI Symposium*, Albuquerque, NM, 2006.
- [3] G. Lerosey, J. de Rosny, A. Tourin, and M. Fink, *Focusing beyond the diffraction limit with far-field time reversal*, *Science* 315 (2007), pp. 1120–1122.
- [4] M. Fink and D. Cassereau, A. Derode, C. Prada, P. Roux, M. Tanter, J. Thomas, and F. Wu, *Time-reversed acoustics*, *Rep. Prog. Phys.* 63 (2000), pp. 1933–1995.
- [5] D. Liu, S. Vasudevan, J. Krolik, G. Bal, and L. Carin, *Electromagnetic time-reversal source localization in changing media: experiment and analysis*, *IEEE Trans Antennas and Propagation* 55 (2007), pp. 344–354.
- [6] A. Ishimaru, S. Jaruwatanaadilok, and Y. Kuga, *Time-reversal effects in random scattering media on super-resolution, shower curtain effects, and backscattering enhancement*, *Radio Sci.* 42 (2007), pp. 1–12.
- [7] J.W. Goodman, *Statistical Optics*, John Wiley, New York, 1985.
- [8] G.T. Ruck, D.E. Barrick, W.D. Stuart, and C.K. Krichbaum, 1970, *Radar Cross Section Handbook*, Plenum Press, New York, 1970.
- [9] A. Ishimaru, *Wave Propagation and Scattering in Random Media*, New York: Academic Press 1997; Piscataway, New Jersey: IEEE Press. Oxford, England: Oxford University Press, 1978.
- [10] A. Taflove and S. Hagness, *Computational Electrodynamics: The Finite Difference Time-Domain Method*. Artech House, Norwood, MA, 2005.